Experimental Section

Chemicals: Copper(II) chloride dihydrate ($CuCl_2 \cdot 2H_2O$, 99.99%), zirconyl chloride octahydrate ($ZrOCl_2 \cdot 8H_2O$, 99.9%) , copper(II) tetra-(4-carboxyphenyl) porphyrin (Cu-TCPP, 95%), tetrakis(4-carboxyphenyl)-porphyrin (TCPP, 98%), and benzoic acid (99.5%) were purchased from Aladdin Biochemical Technology Co., Ltd. Acetone, ethanol, and N, N-dimethylformamide (DMF, 99.8%) were obtained from Kermel Chemical Reagent Co., Ltd. Potassium hydroxide (KOH, 85%)) was obtained from Sinopharm Chemical Reagent Co., Ltd., P. R. China. Cesium hydroxide (CsOH, 99%), sodium hydroxide (NaOH, 96%) and deuterium oxide (D_2O, 99.9%) were bought from InnoChem Technology Co., Ltd. Anion exchange membrane (Fumasep FAB-PK-130) and polytetrafluoroethylene-hydrophobized carbon paper (PTFE-CP, Toray, YLS-30T GDL) were purchased from Suzhou Sinero Technology Co., Ltd. Nafion D-520 (5 wt%) dispersion was obtained from Alfa Aesar China Co., Ltd. Cellulose microgel (CMG) was provided by Green Micro & Nano Technology Co., Ltd. (GMN, Hangzhou China). CO_2 (99.999%) and Ar (99.99%) were acquired from Henan Yuanzheng Technology Co., Ltd.

The synthesis of the PMOF catalyst: In a typical procedure[1], 10 mL of DMF, 30 mg of $ZrOCl_2 \cdot 8H_2O$, 280 mg of benzoic acid, 10 mg of TCPP and 100 μL of H_2O were dissolved by ultrasonic treatment for 30 min. Next, the resulting solution was transferred to a Teflon-lined autoclave (20 mL), which was then heated at 90 °C for 8 h. Subsequently, the products were separated via centrifugation and further washed with H_2O and ethanol multiple times to remove impurities. The obtained products were dried for 12 h in a vacuum oven at ambient temperature. The resulting powder was named as the PMOF catalyst.

The synthesis of the Cu-PMOF catalyst: In a typical procedure[2], the obtained PMOF powders (20 mg) and $CuCl_2 \cdot 2H_2O$ aqueous solution (30 mg mL^{-1}, 200 μL) were added to 4 mL of DMF. The above mixture underwent stirring at ambient temperature for 10 min and then was transferred to a 10 mL Teflon-lined autoclave, which was heated at 80 °C for 4 h. Next, the products were separated through centrifugation and further washed with ethanol multiple times. Subsequently, the obtained products were dried under vacuum at 80 °C and referred to as the Cu-PMOF catalyst.

The synthesis of Cu-PMOF-1 and Cu-PMOF-2 catalysts: The Cu-PMOF-1 and Cu-PMOF-2 were prepared by the same method of the Cu-PMOF catalyst synthesis except that the concentration of $CuCl_2 \cdot 2H_2O$ solution was 15 and 100 mg mL^{-1}, respectively.

The preparations of different working electrodes: In a typical procedure[2], the ink was the mixed solution of the catalyst (5 mg, including PMOF, Cu-PMOF, Cu-PMOF-1, Cu-PMOF-2, and Cu-TCPP), acetone (1 mL), and CMG (30 μL). The resulting mixture underwent ultrasonic treatment for 30 min to form a uniform catalyst ink. To obtain the working electrode, the as-prepared ink was

uniformly sprayed on the PTFE-CP, and the electrode was dried for 2 h in a vacuum oven at ambient temperature prior to subsequent electrochemical measurements. The preparation method for the Cu-PMOF/Nafion electrode was identical to that of the Cu-PMOF electrode, with the sole modification being the substitution of CMG with Nafion D-520 dispersion.

Characterizations: Morphological and structural analyses of PMOF, Cu-TCPP, Cu-PMOF, Cu-PMOF-1, and Cu-PMOF-2 catalysts were conducted by a Carl Zeiss SIGMA 500 scanning electron microscope (SEM) and a Tecnai G2 F20 high-resolution transmission electron microscopy (TEM) with energy dispersive X-ray spectroscopy (EDS). The X-Ray diffraction (XRD) patterns of various catalysts were performed on a X'Pert PRO X-ray diffractometer with Cu-Kα radiation (λ = 0.15406 nm) with the scan speed of 5° min^{-1}. The high-angle annular dark-field scanning transmission electron microscopy (HAADF-STEM) image of the Cu-PMOF catalyst was acquired via a JEM-ARM300F microscope equipped with EDS. The X-ray photoelectron spectroscopy (XPS) spectra of different catalysts were carried out on Thermo Scientific ESCALab 250Xi with C 1s line at 284.8 eV for energy standard. Inductively coupled plasma-optical emission spectrometry (ICP-OES, Vista-MPX) was employed to determine the elemental composition of Cu-PMOF, Cu-PMOF-1, and Cu-PMOF-2 catalysts. The ATR mode of a PerkinElmer spectrometer was utilized to measure the Fourier transform infrared (FTIR) spectra. The X-ray absorption spectroscopy (XAS) analyses of the Cu-PMOF catalyst, Cu foil, Cu_2O and CuO were obtained at the 1W2B beamline of Beijing Synchrotron Radiation Facility (BSRF) in China. The extended X-ray absorption fine structure (EXAFS) data were processed based on the standard procedures using the ATHENA module implemented in the IFEFFIT software packages.

Electrocatalytic CO_2 reduction: In this study, electrochemical measurements were performed on the CorrTest CS3104 electrochemical workstation (Wuhan CorrTest Instruments Co., Ltd.). A typical electrochemical flow cell was employed for the experiment, which integrated a gas compartment, a cathodic chamber, and an anodic chamber (Figure S9). The anodic and cathodic chambers were separated by an anion exchange membrane (Fumasep FAB-PK-130). A three-electrode system was employed, consisting of a Hg/HgO reference electrode (1 M KOH), a Pt foil counter electrode, and a working electrode (PMOF, Cu-TCPP, Cu-PMOF, Cu-PMOF-1, or Cu-PMOF-2). Systematic electrolysis tests were carried out at fixed current densities (-100, -200, -300, -400, and -500 mA cm^{-2}) for 30 min in 1 M KOH electrolyte under continuous CO_2 flow. All applied potentials were translated to the reversible hydrogen electrode (RHE) scale by $E_{\mathrm{RHE}} = E_{\mathrm{Hg/HgO}} - 80\% \times i \times R_{cell} + 0.098\ \mathrm{V} + 0.0591 \times pH$[3, 4]. During the electrochemical experiment, both the catholyte and anolyte were 1 M KOH aqueous solutions (30 mL), with a circulation rate of 60 mL min^{-1}. Meanwhile, a digital gas flow controller was employed to maintain

the CO_2 gas flow rate at 20 sccm into the gas compartment, and the outlet gas flow rate was also monitored with a high-precision mass flow meter. Linear sweep voltammetry (LSV) curves of different electrodes were recorded in 1 M KOH solution under flowing CO_2 or Ar. The potential was swept from 0 to -1.3 V *versus* RHE with a scan rate of 5 mV s^{-1}.

Electrochemical impedance spectroscopy (EIS) measurements were performed at an open circuit potential (OCP) over a frequency range of 100 kHz to 0.1 Hz, with an applied amplitude of 10 mV. Given the direct proportionality between the double-layer capacitance (C_{dl}) value and the electrochemical active surface area (ECSA),[3, 5] C_{dl} value of different electrodes were determined to evaluate their ECSAs. Cyclic voltammetry (CV) measurements were performed in a non-faradaic potential window of 0.15 to 0.25 V *versus* RHE at scan rates ranging from 140 to 300 mV s^{-1}. To quantify the C_{dl}, the difference between anodic and cathodic current densities ($\Delta j = j_a - j_c$) measured at 0.10 V *versus* RHE was plotted as a function of scan rate, with j_a and j_c representing the anodic and cathodic current densities, respectively.

Gaseous and liquid products analysis: Gas products generated during the electrolysis reaction were collected and analyzed using a gas chromatograph (GC, Agilent 8860), which featured a thermal conductivity detector (TCD) for detecting H_2, CO and CH_4, and a flame ionization detector (FID) for analyzing hydrocarbon species. The liquid product was detected by ^{1}H NMR analysis in D_2O using a Bruker Advance III 500 HD spectrometer. The calculation formula of the Faradaic efficiency (FE) for different products are presented as follows[2]:

$$\text{FE (\%)} = \frac{z \times n \times F}{\text{Q}} \times 100\%$$

Where z represents the number of electrons transferred for the formation of the product, n denotes the mole of product; F is Faraday constant (96,485 C mol^{-1}); Q denotes the amount of charge accumulated during the electrocatalytic CO_2 reduction.

***In situ* Raman Spectroscopy:** A confocal Raman spectrometer (Horiba LabRAM Odyssey) with a 532 nm laser source was used to acquire *in situ* Raman spectra. The measurements were performed using a customized spectro-electrochemical flow cell, allowing real-time detection of the GDL through a quartz window. For each measurement, the Raman spectrum was acquired by integrating two consecutive 20-second acquisitions. A syringe pump was utilized to continuously flow the electrolyte (1 M KOH) over the GDL with a rate of 20 mL min^{-1}. CO_2 was delivered to the backside of the GDL. Potentials were applied in controlled potential holds relative to a Hg/HgO reference electrode and later converted to the RHE scale. Spectroscopic measurements were conducted at the open circuit potential (OCP) and across a potential range of -0.6 V to -1.2 V *versus* RHE, using Pt foil as the counter electrode to ensure a stable electrochemical environment.

***In situ* attenuated total reflection surface enhanced infrared absorption spectroscopy (ATR-**

SEIRAS): The ATR-configured SEIRAS was utilized for the electrochemical measurements. The experiments were carried out on a Thermo Nicolet Is50 spectrometer, which was equipped with a mercury cadmium telluride (MCT) detector cooled by liquid nitrogen. A gold (Au) thin film (~60 nm) was deposited onto a silicon (Si) prism via a two-step wet chemical procedure. Subsequently, the ink solution (30 μL) was deposited onto the Au film-coated working electrode and then the obtained prism as the working electrode was assembled into a homemade spectro-electrochemical cell for *in situ* ATR-SEIRAS measurements. The Ag/AgCl was reference electrode, which was introduced near the working electrode, and the Pt mesh (1 cm × 1 cm) was serve as the counter electrode. CO_2 was continuously bubbled into the 0.5 M $KHCO_3$ electrolyte during *in situ* ATR-SEIRAS measurements. All infrared spectra were recorded after maintaining a constant potential across the electrode for 5 min. The background spectrum was subtracted from each spectrum prior to the measurements. Initially, the infrared spectrum was recorded at OCP, after which reaction spectra were measured within the potential range of -0.5 V to -1.4 V *versus* RHE.

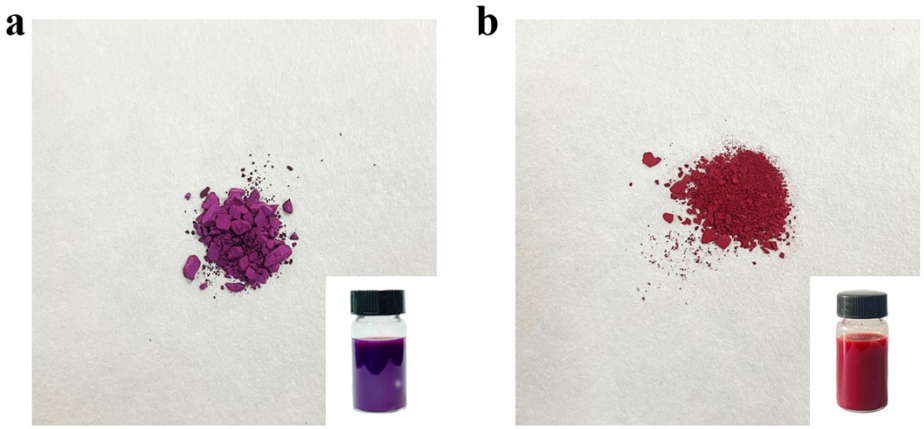

Figure S1. The photographs of different catalysts: (a) PMOF and (b) Cu-PMOF.

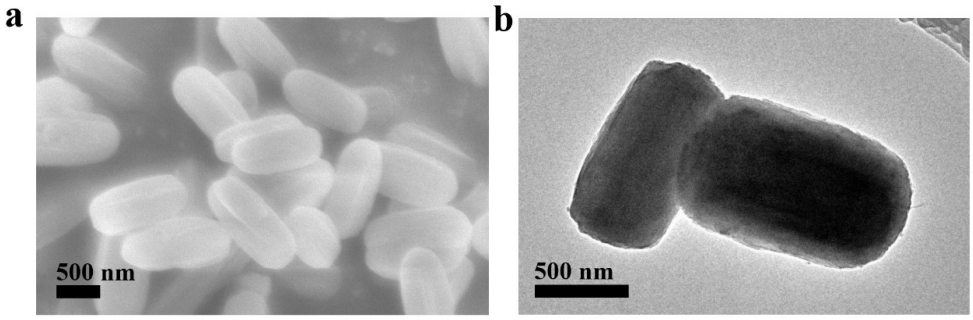

Figure S2. (a) The SEM image of the PMOF catalyst; (b) The TEM image of the PMOF catalyst.

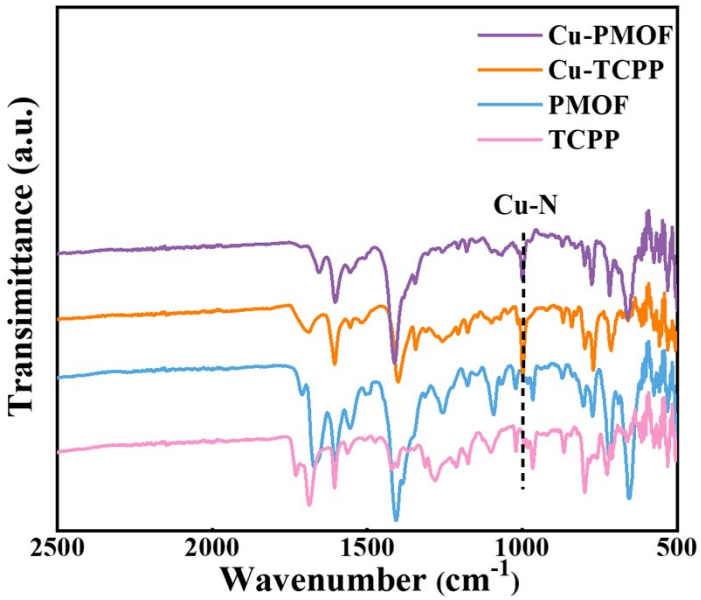

Figure S3. FTIR spectra of PMOF, Cu-PMOF, Cu-TCPP and TCPP samples.

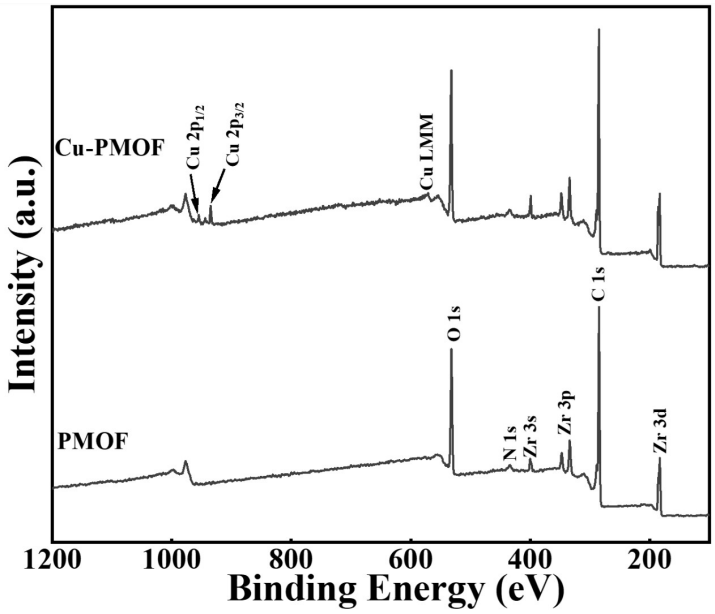

Figure S4. The XPS spectra of Cu-PMOF and PMOF catalysts.

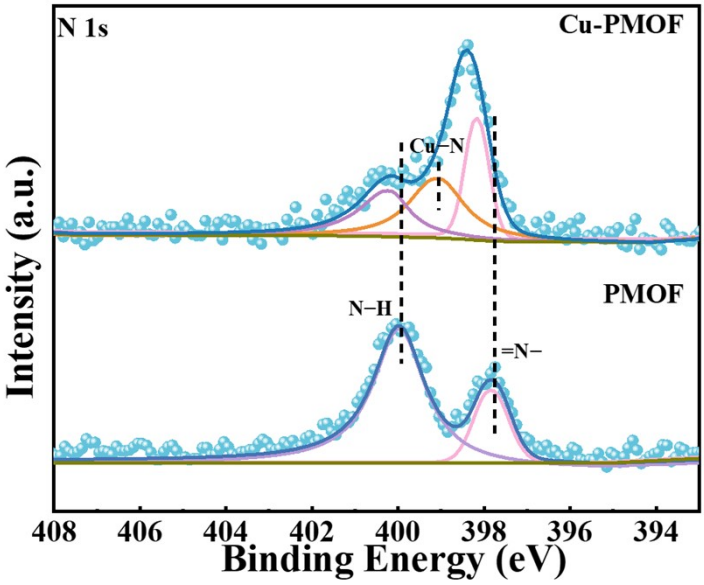

Figure S5. N 1s XPS spectra of PMOF and Cu-PMOF catalysts.

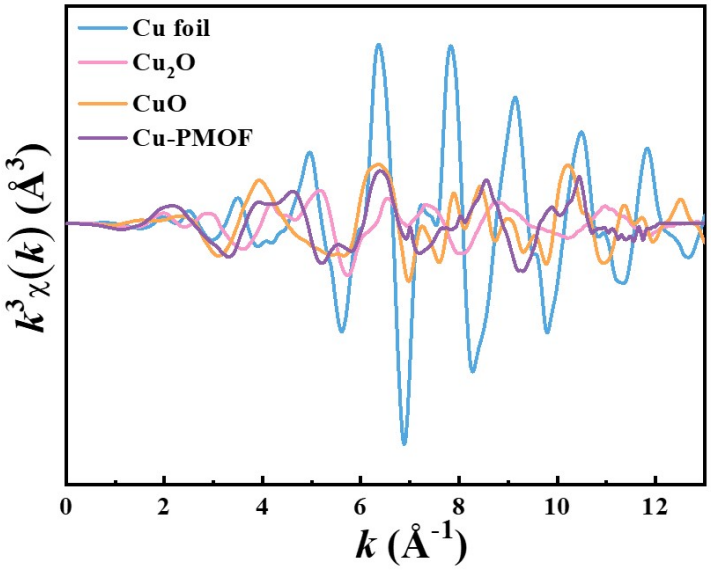

Figure S6. Cu K-edge extended EXAFS oscillation function k^2c(k) for Cu-PMOF, Cu foil, Cu_2O, and CuO samples.

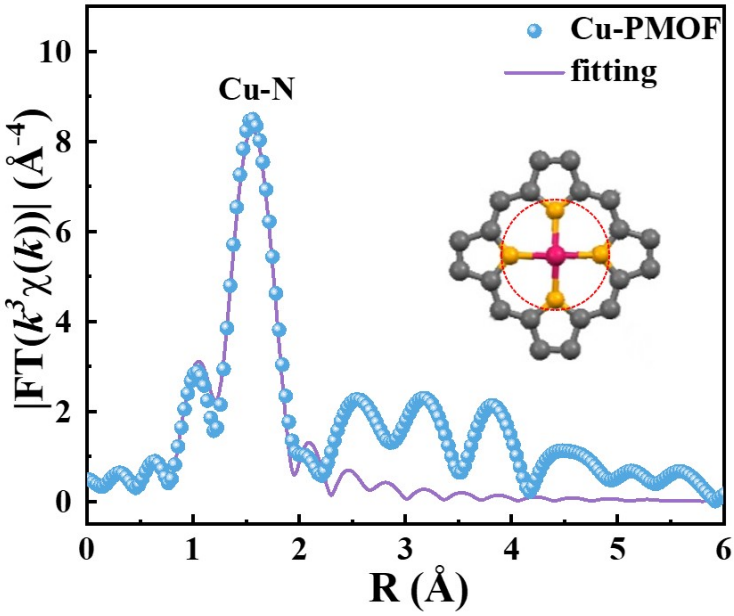

Figure S7. The EXAFS fitting results of the Cu-PMOF catalyst. The inset image is the structure of Cu sites in the Cu-PMOF catalyst.

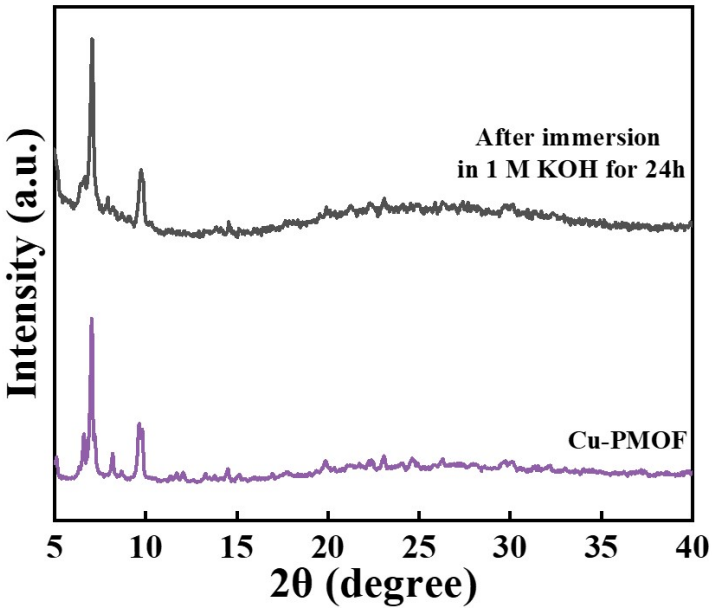

Figure S8. The PXRD patterns of the Cu-PMOF catalyst before and after immersion in 1 M KOH for 24 h.

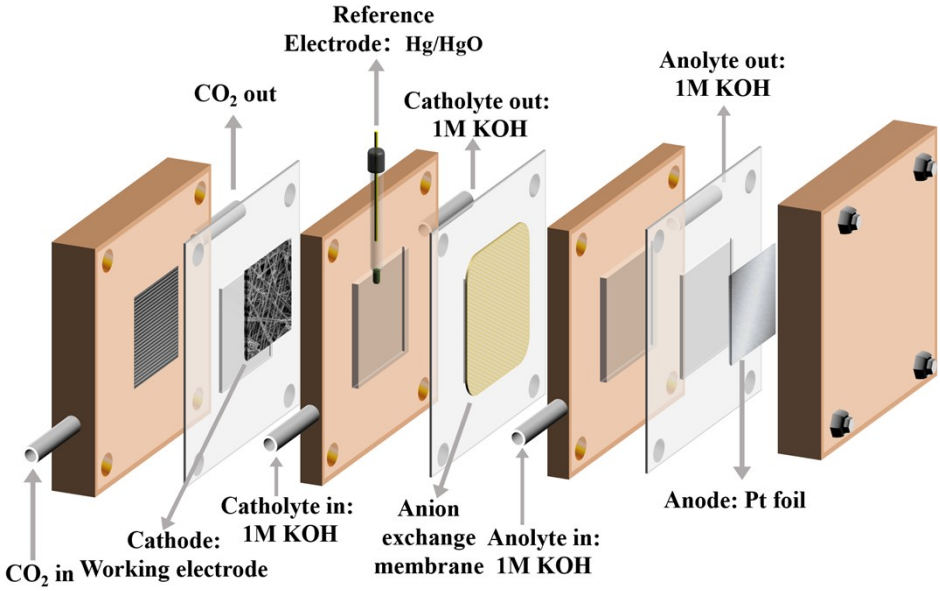

Figure S9. Schematic diagram of the flow cell structure.

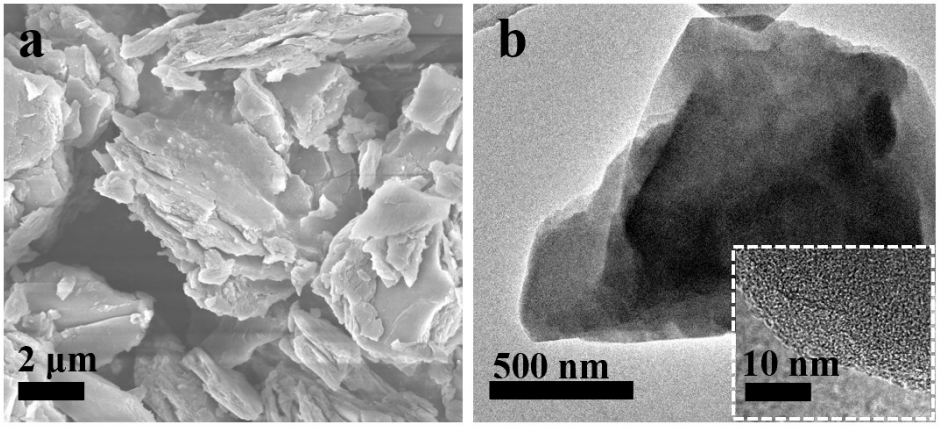

Figure S10. (a) The SEM image of the commercial Cu-TCPP; (b) The TEM image of the commercial Cu-TCPP. The inset image is the HR-TEM image of the commercial Cu-TCPP.

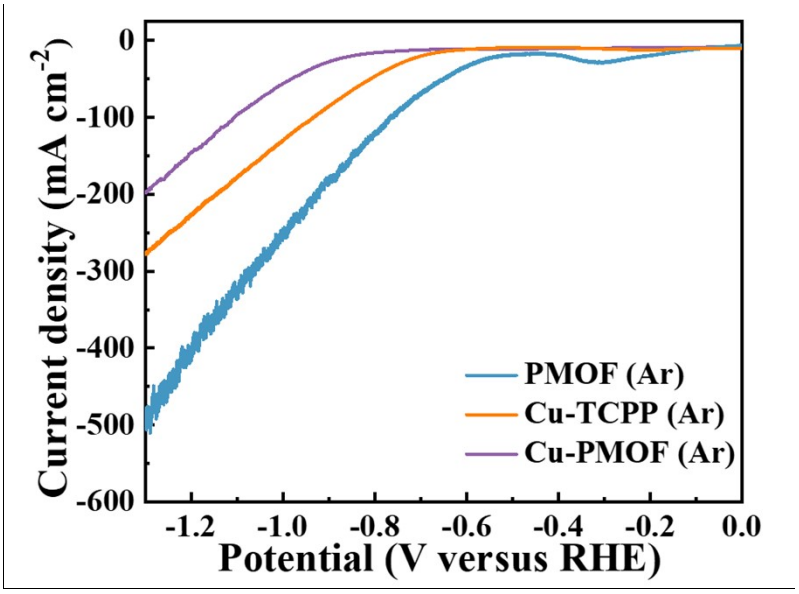

Figure S11. LSV curves of Cu-PMOF, PMOF, and Cu-TCPP electrodes in 1 M KOH electrolyte with Ar flow.

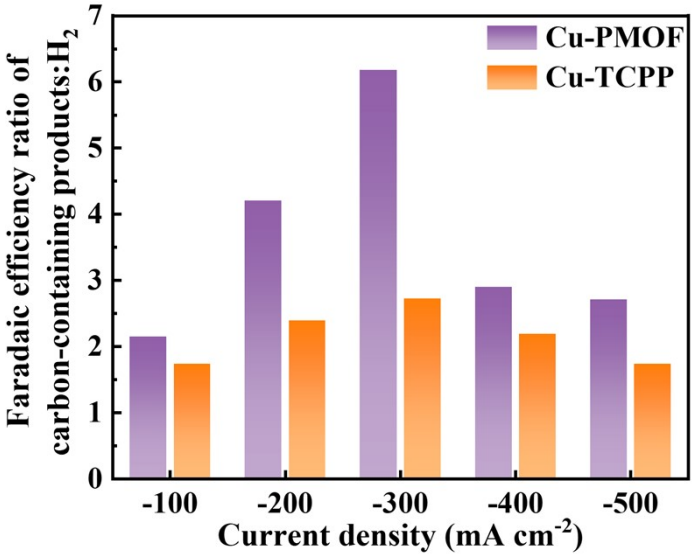

Figure S12. The Faradaic efficiency of carbon-containing products and H_2 ratios for Cu-PMOF and Cu-TCPP electrodes at different current densities.

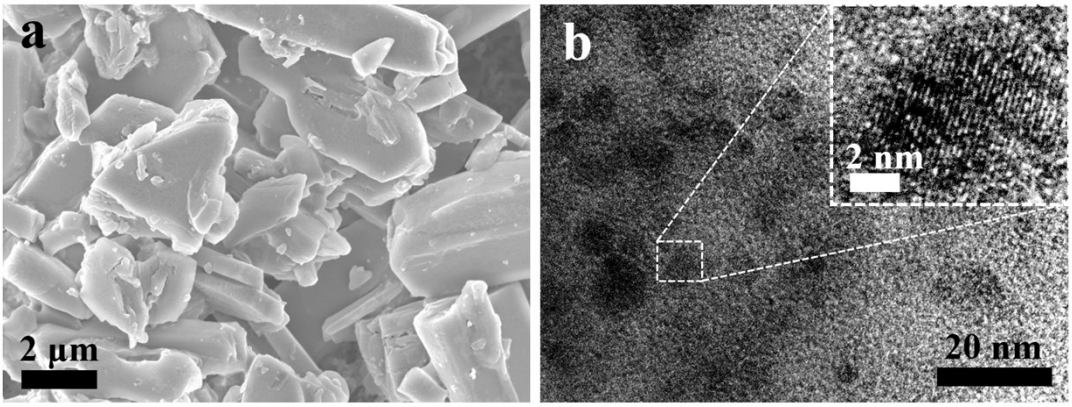

Figure S13. (a) The SEM image of the Cu-TCPP electrode after electrolysis; (b) The TEM image of the Cu-TCPP electrode after electrolysis (The inset image is the HR-TEM image of the Cu-TCPP electrode after electrolysis).

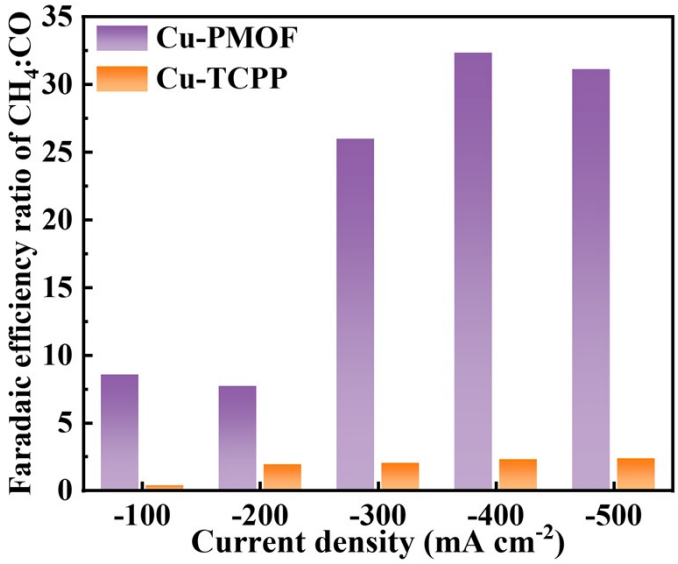

Figure S14. The Faradaic efficiency ratios of CH_4:CO for Cu-PMOF and Cu-TCPP electrodes at different current densities.

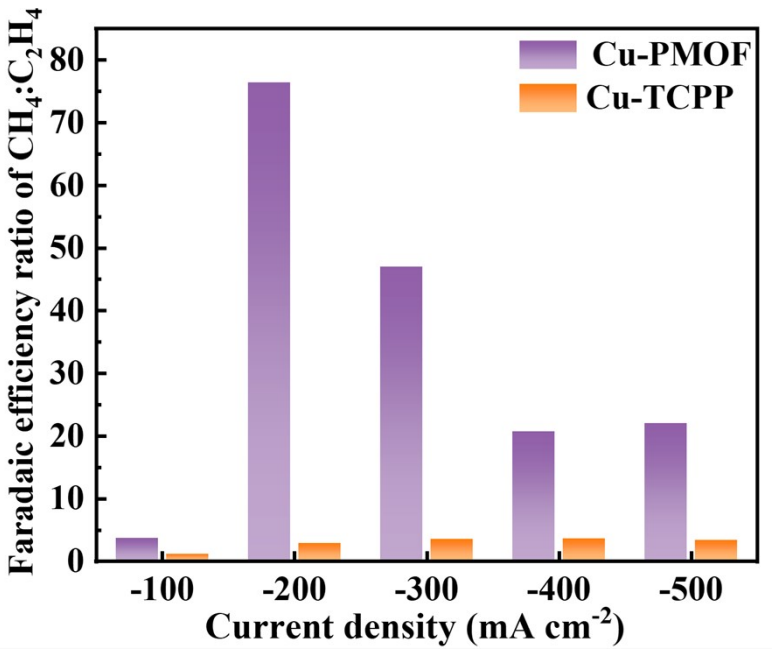

Figure S15. The Faradaic efficiency ratios of CH_4:C_2H_4 for Cu-PMOF and Cu-TCPP electrodes at different current densities.

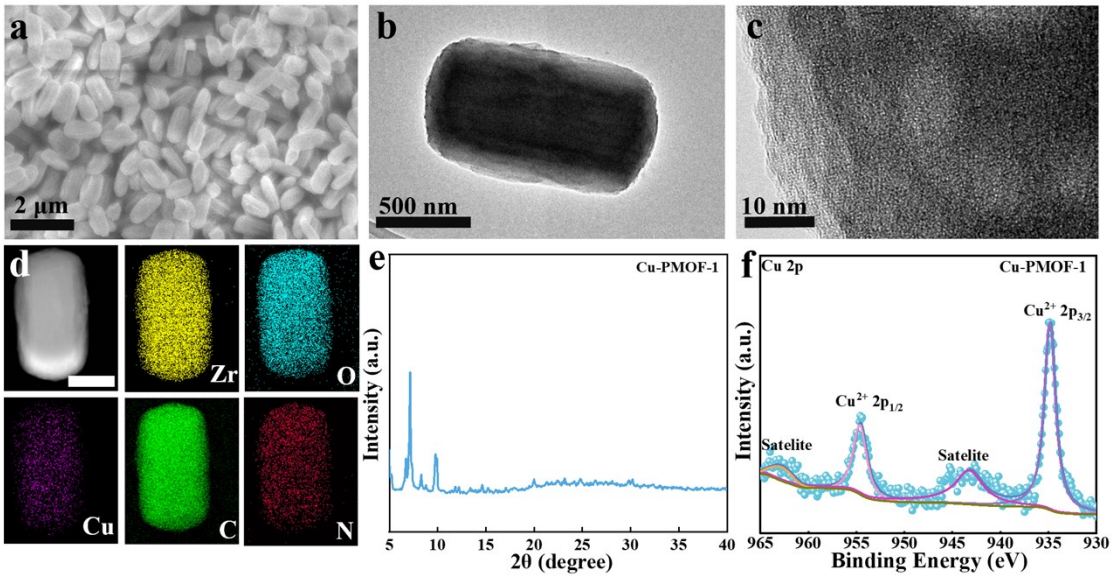

Figure S16. The characterization results of the Cu-PMOF-1 catalyst: (a) the SEM image, (b) the TEM image, (c) the HR-TEM image, (d) EDS mapping images (Scale bar = 500 nm), (e) the PXRD pattern, and (f) the Cu 2p XPS spectrum.

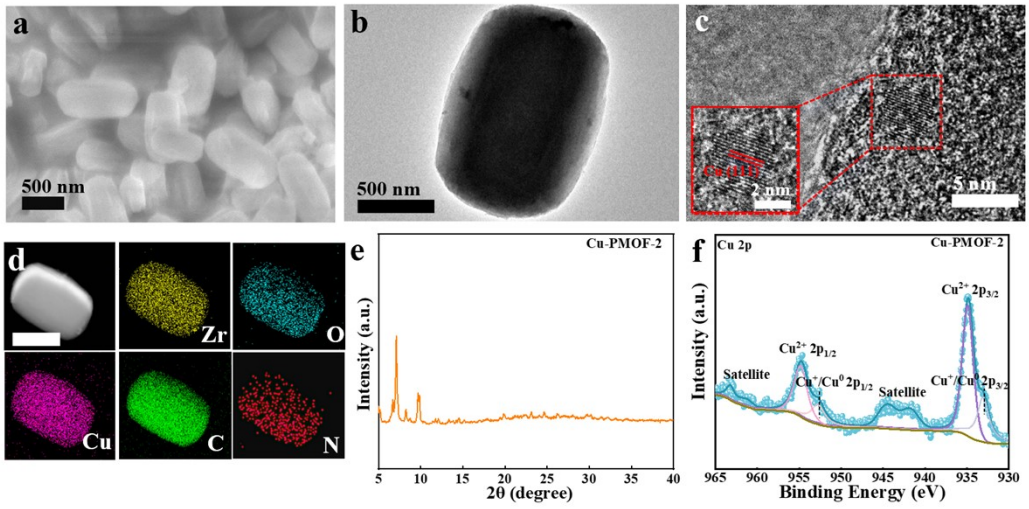

Figure S17. The characterization results of the Cu-PMOF-2 catalyst: (a) the SEM image, (b) the TEM image, (c) the HR-TEM image, (d) EDS mapping images (Scale bar = 500 nm), (e) the PXRD pattern, and (f) the Cu 2p XPS spectrum.

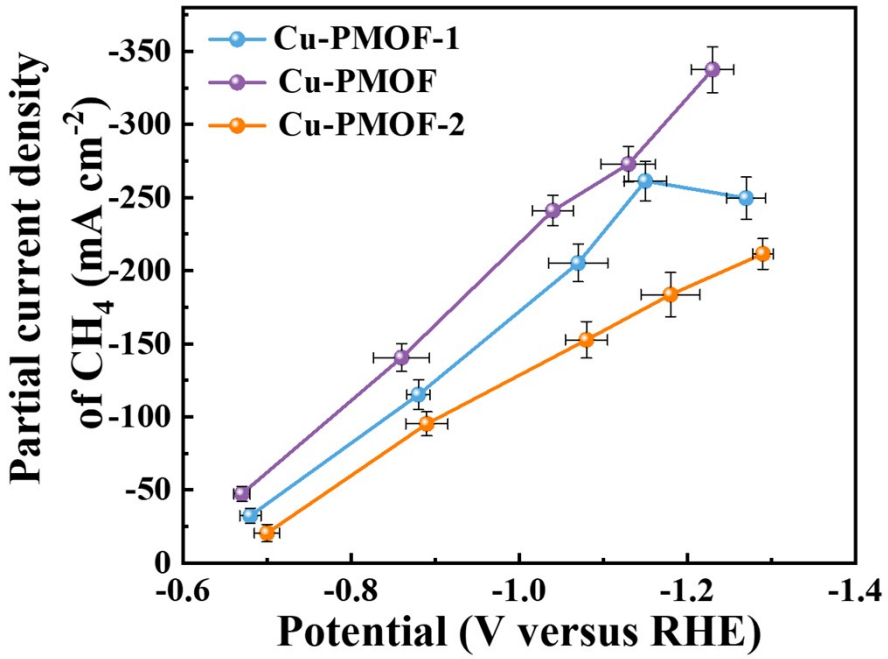

Figure S18. The partial current density of CH_4 at different applied potentials on Cu-PMOF-1, Cu-PMOF and Cu-PMOF-2 electrodes.

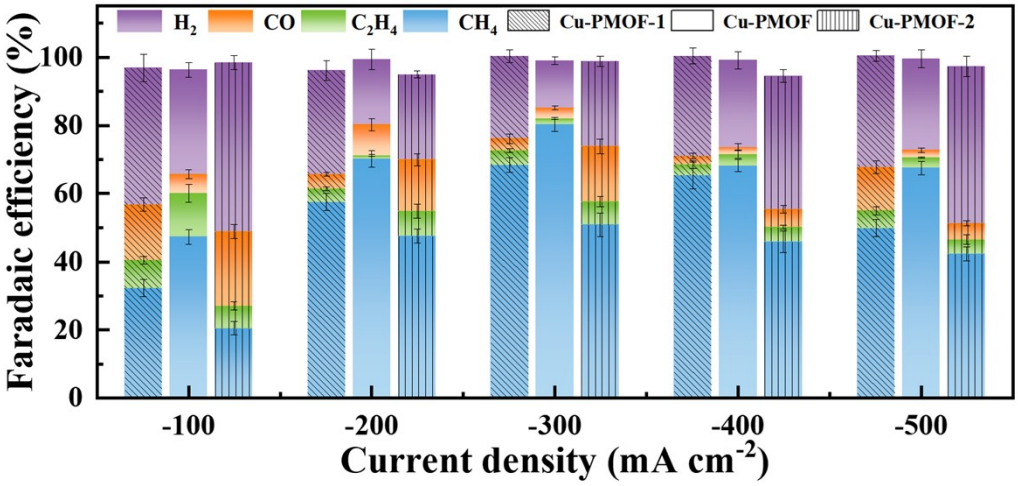

Figure S19. The Faradaic efficiency of various products at different current densities on Cu-PMOF-1, Cu-PMOF and Cu-PMOF-2 electrodes.

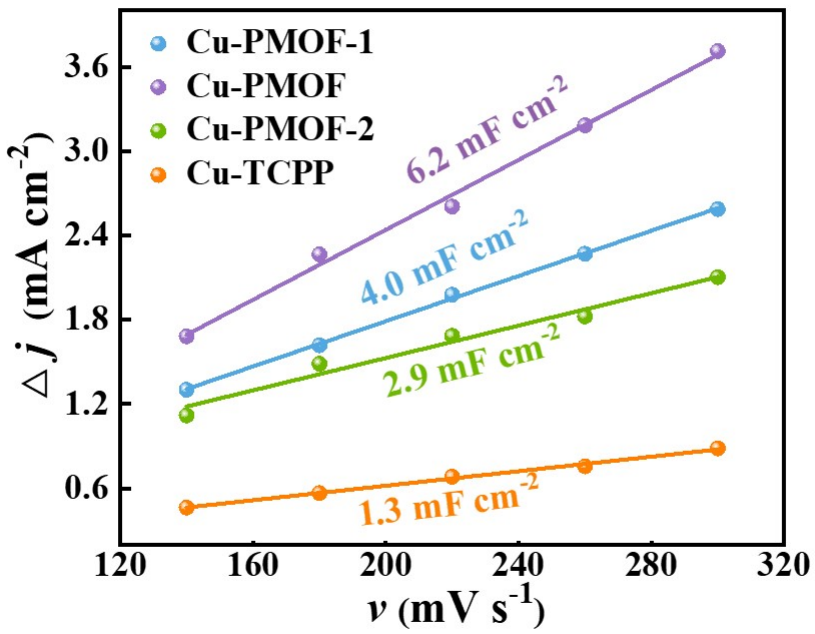

Figure S20. Charging current densities against scan rates over various electrodes.

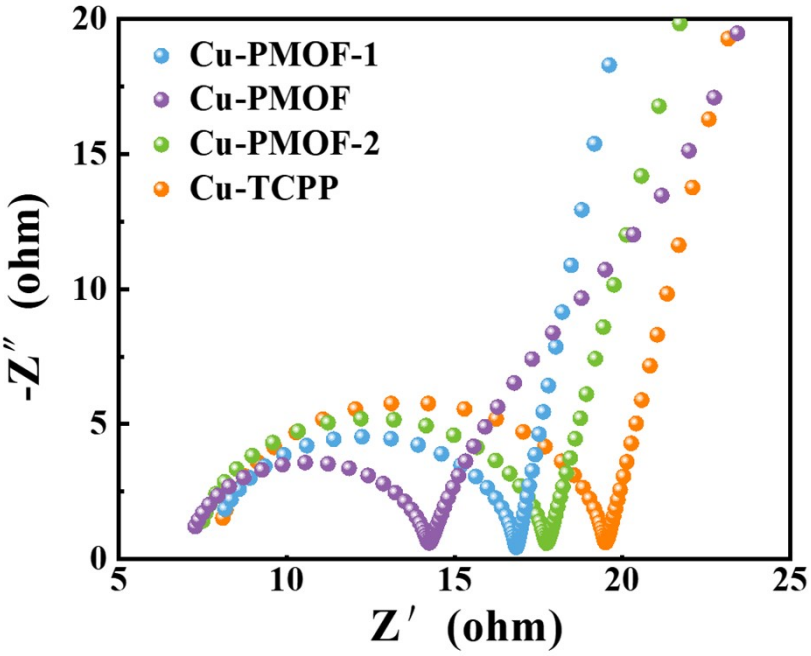

Figure S21. Nyquist plots of different electrodes.

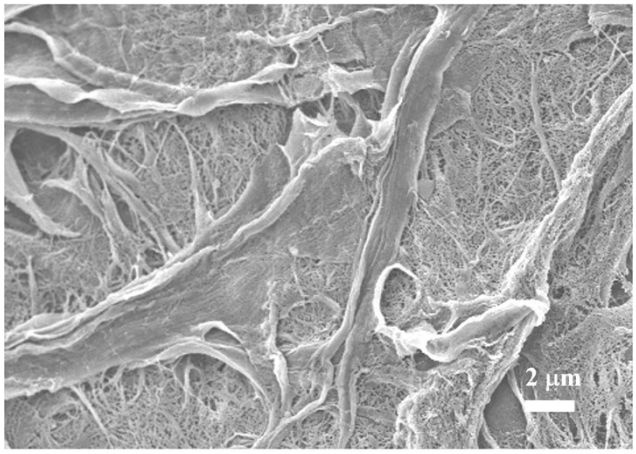

Figure S22. The SEM image of the CMG.

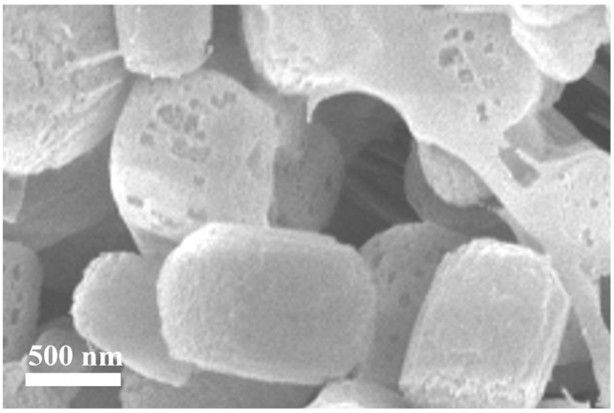

Figure S23. The SEM image of the Cu-PMOF electrode with the CMG.

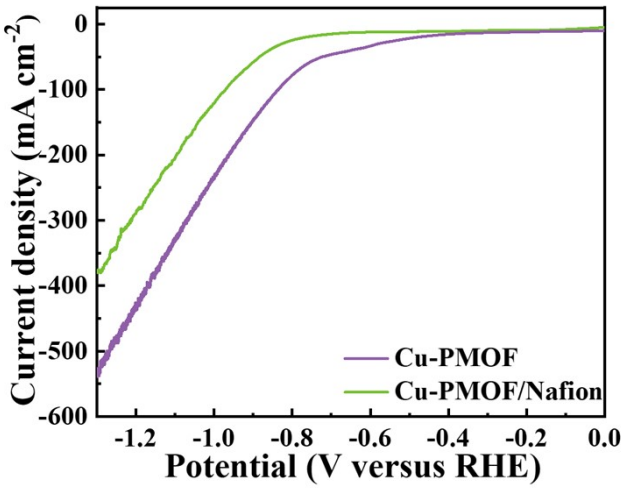

Figure S24. LSV curves of Cu-PMOF and Cu-PMOF/Nafion electrodes in a 1 M KOH electrolyte with CO_2 flow.

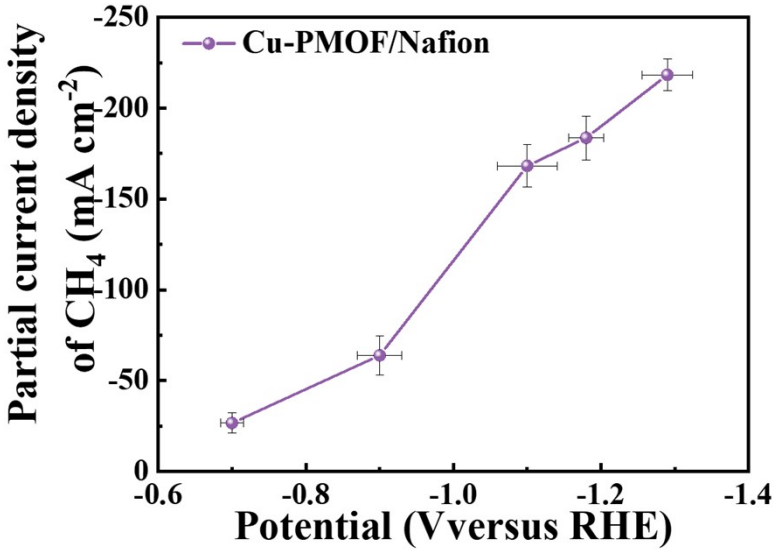

Figure S25. The partial current density of CH_4 at different applied potentials on the Cu-PMOF/Nafion electrode.

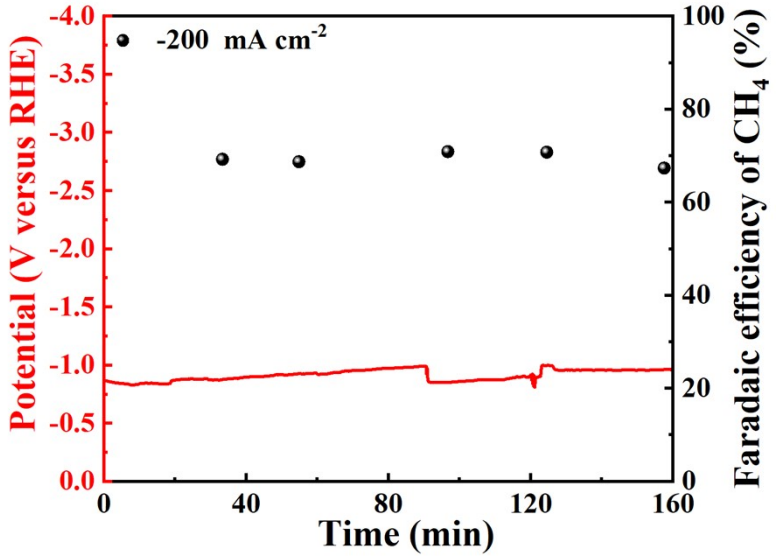

Figure S26. The long-term stability test of the Cu-PMOF electrode in a 1 M KOH electrolyte with a constant current density of -200 mA cm^{-2}.

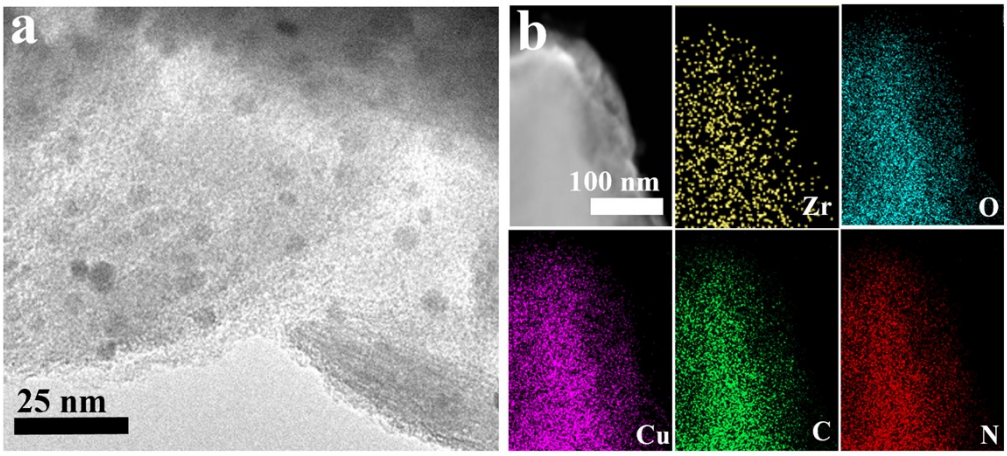

Figure S27. (a) The TEM image of the Cu-PMOF electrode after electrolysis; (b) The EDS mapping images of the Cu-PMOF electrode after electrolysis.

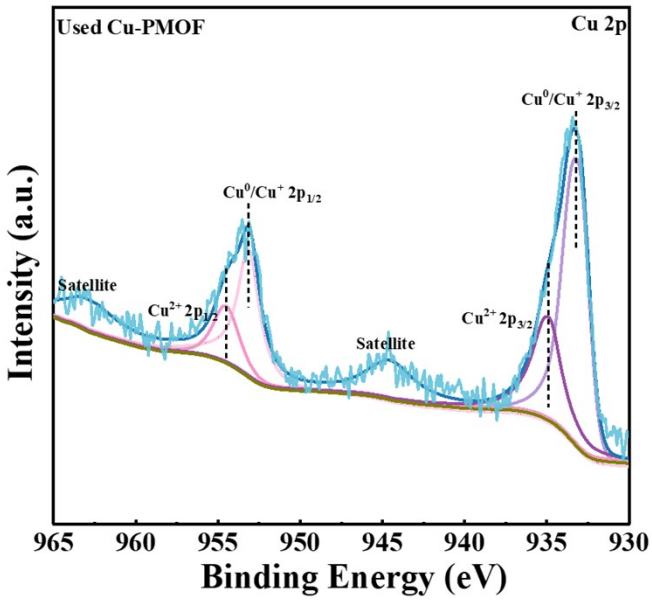

Figure S28. The Cu 2p XPS spectrum of the used Cu-PMOF electrode.

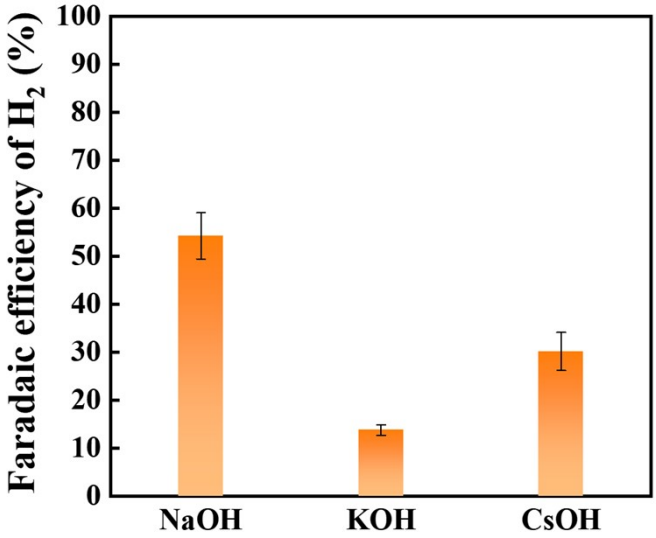

Figure S29. The Faradaic efficiency of H_2 on the Cu-PMOF electrode with a current density of -300 mA cm^{-2} in different electrolytes.

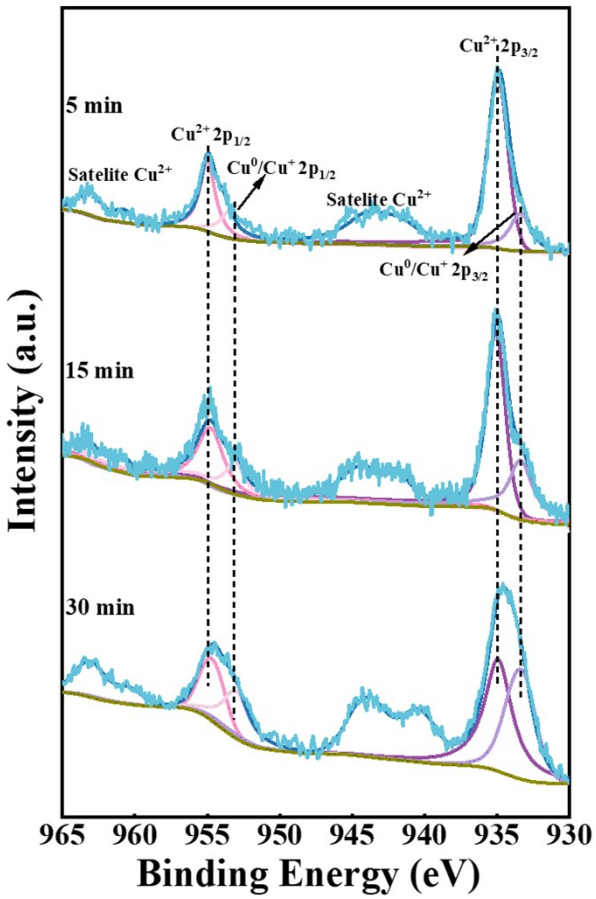

Figure S30. Cu 2p XPS spectra of Cu-PMOF electrodes after 5 min, 15 min, and 30 min of electrolysis.

Table S1. The Cu loading amount in different catalysts determined by ICP-OES results.

Catalyst	Cu (wt%)
Cu-PMOF-1	2.9
Cu-PMOF	3.5
Cu-PMOF-2	5.2

Table S2. Structure parameters of various samples obtained from EXAFS fitting results at Cu K-edge.

Sample	Shell	CN[a]	R(Å)[b]	σ^2(Å^2)[c]	ΔE_0(eV)[d]	R factor
Cu-PMOF	Cu-N	4.0±0.2	1.98±0.01	0.0032± 0.0004	6.9±0.8	0.0090
Cu foil	Cu-Cu	12.±0.2	2.54±0.02	0.0087± 0.0004	4.3±0.8	0.0023
Cu_2O	Cu-O	4.0±0.2	1.86±0.02	0.0035± 0.0004	10.2±0.8	0.0041
CuO	Cu-O	4.0±0.2	1.96±0.02	0.0047±0.0004	-0.7±0.8	0.0063

[a] CN, coordination number; [b] R, distance between absorber and backscatter atoms; [c] σ^2, Debye-Waller factor to account for both thermal and structural disorders; [d] ΔE_0, inner potential correction; R factor indicates the goodness of the fit. S_0^2 was fixed to 0.98, according to the experimental EXAFS fit of Cu foil by fixing CN as the known crystallographic value. A reasonable range of EXAFS fitting parameters: $0.700 < S_0^2 < 1.000$; CN > 0; σ^2Å$^2 > 0$; $|\Delta E_0| < 15$ eV; R factor < 0.02.

Table S3. Values of C_{dl} and EIS parameters of different electrodes.

Electrode	C_{dl} (mF cm^{-2})	R_{ct} (Ω cm^{-2})
Cu-PMOF	6.2	7.2
Cu-PMOF-1	4.0	8.7
Cu-PMOF-2	2.9	10.2
Cu-TCPP	1.3	11.4

Table S4. The electrocatalytic performance of state-of-the-art catalysts for the electrocatalytic CO_2 reduction to CH_4.

Catalyst	Faradaic efficiency of CH_4 (%)	Partial current density of CH_4 (mA cm^{-2})	Applied potential (V *versus* RHE)	electrolyte	Cell Type	Ref.
Cu-PMOF	80.4	-241.2	-1.04	1 M KOH	Flow cell	This work
CuTCPP NFs[a]	61	-18.8	-1.30	0.1 M $KHCO_3$	H-Type	[6]
CPFs[b]	56	-7.5	-1.40	0.1 M $KHCO_3$	H-Type	[7]
CuTAPP[c]	54.8	-290.5	-1.63	1 M KOH	Flow cell	[8]
Cu-TDPP-NS[d]	70	-180.3	-1.60	0.5 M PBS[e]	Flow cell	[9]
Cu-Tph-COF-Dct[f]	80	-220	-0.90	1 M KOH	Flow cell	[10]
La-2Cu-NiPc-DHDA-COF[g]	51.7	-188.5	-1.70	1 M KOH	Flow cell	[11]
Por-Cu[h]	44	-14.2	-0.98	0.5 M $KHCO_3$	H-Type	[12]
Cu-N-5%-400[i]	42	-100	-1.00	1 M KOH	Flow cell	[13]
Cu-CDs[j]	78	-40	-1.44	0.5 M $KHCO_3$	H-Type	[14]
Cu_{SA}-N_2/C[k]	83.5	-16.6	-1.45	0.5 M $KHCO_3$	H-Type	[15]
NC-SA Cu/COF[l]	56.2	-19.2	-1.26	0.1 M $KHCO_3$	H-Type	[16]
CuPc[m]	66	-13	-1.6	0.5 M $KHCO_3$	H-Type	[17]
4:1 ratio of CNP to CuPc[n]	62	-136	-4.00 V[o]	1 M KOH	MEA[p]	[18]
$Cu_{0.05}$-CN[q]	49	-8.0	-1.2	0.1 M $KHCO_3$	H-Type	[19]
CuPPc[r]	55	-18	-1.25	0.1 M $KHCO_3$	H-Type	[20]
CuNC-700[s]	50.7	-304.2	-1.6	1 M KOH	Flow cell	[21]
2Bn-Cu@UiO-67[t]	81	-340.2	-1.5	1 M KOH	Flow cell	[22]
Cu SAs-0.1[u]	68.2	-493.1	-1.8	1 M KOH	Flow cell	[23]
Cu-PTI[v]	68	-348	-0.84	1 M KOH	Flow cell	[24]
BNC-Cuw[w]	73	-462	-1.94	1 M KOH	Flow cell	[25]
Cu NPs from Cu-MOF-74[x]	50	-5	-1.30	0.1 M $KHCO_3$	Flow cell	[26]

Cu-N/IPCF[y]	74.2	-222.6	-1.21	1 M KOH	Flow cell	5
Cu-DBC[z]	80	-203	-0.9	1 M KOH	Flow cell	27
Cu-PzI[aa]	52	-287.5	-0.9	1 M KOH	Flow cell	28
Cu SA/F-GDY[ab]	72.3	-174.2	-1.2	1 M KOH	Flow cell	29
Cu SAs/HGDY[ac]	72.1	-230.1	-1.1	1 M KOH	Flow cell	30
La_5Cu_{95}[ad]	64.5	-193.5	-1.72	1 M KOH	Flow cell	31
Cu-CeO_2-4%[ae]	58	-56	-1.80	0.1 M $KHCO_3$	H-Type	32
Cu/CeO_2-x HDs[af]	54	-2.1	-1.20	0.1 M $KHCO_3$	H-Type	33
La_2CuO_4[ag]	56.3	-117	-1.40	1 M KOH	Flow cell	34
	62	-4.2	-1.30	0.1 M $KHCO_3$	H-Type	34
Cu/p-Al_2O_3 SAC[ah]	62	-153	-1.20	1 M KOH	Flow cell	35
Cu/CeO_2-R[ai]	49.3	-22	-1.6	0.1 M $KHCO_3$	H-Type	36
Cu-N-P[aj]	73	146	-1.6	1 M KOH	Flow cell	37

[a] CuTCPP nanoflowers; [b] Cu-porphyrin-constructed porous frameworks; [c] 5,10,15,20-tetrakis(4-aminophenyl) porphyrin Cu(II) (CuTAPP); [d] Cu-porphyrin-based large-scale (~1.5 μm) and ultrathin nanosheet (~5 nm); [e] phosphate buffer solution; [f] Cu-Tph-covalent organic frameworks (-2, 4-diamino-6-cholo-1,3, 5-triazine, denoted as Dct) [g] nickel(II) 2,3,9,10,16,17,23,24-octakis(amino)phthalocyanine ($(NH_2)_8NiPc$) and 1,8-dihydroxynaphthalene-2,7-dicarbaldehyde (DHDA); [I] Cu single bond N composite catalyst embedded in a carbon matrix-400 °C; [j] Cu-embedded carbon dots; [k] asymmetric Cu-N_2 sites;[l] Cu nanoclusters and Cu single atoms covalent organic frameworks (COFs); [m] Cu(II) phthalocyanine; [n] carbon nanoparticle (CNP) Cu(II) phthalocyanine (CuPc); [o] -4.00 V *versus* Ag/AgCl; [p] membrane electrode assembly; [q] Cu single atoms loaded in g-C_3N_4 catalysts; [r] conjugated Cu phthalocyanine polymer; [s] Cu doped carbon catalyst (CuNC) derived from a metal-organic framework (MOFs)-700°C; [t] N-heterocyclic carbene (NHC)-ligated Cu single atom site embedded in MOF; [u] Cu single-atom catalysts (0.01 stand for percentage); [v] Li-polytriazine imides (PTI); [w] nearest neighbor structure of isolated Cu sites with boron dopant (BNC-Cu); [x] Cu nanoparticles (NPs) were derived from Cu-based MOF-74; [y] interconnected mesoporous carbon fiber (IPCF) stabilizing isolated Cu-N_3 moieties; [z] Cu-based conductive MOF (dibenzo-[g,p]chrysene-2,3,6,7,10,11,14,15-octaol, 8OH-DBC); [aa] omomorphic one-dimensional (1D) chain compounds, $[Cu(4\text{-}XPz)_2]_n$ solvent, (X=H, Cl, Br, I; Pz=pyrazole); [ab] Cu single-atom F-substituted graphdiyne; [ac] meta-position structure of alkynyl in 1,3,5-triethynylbenzene and the interaction between Cu and −C≡C−, a Cu SAs electrocatalyst; [ad] alloying Cu with oxophilic metal (M); [ae] low concentration (<5%) Cu species in CeO_2 nanorods; [af] Cu/CeO_2-x nanocrystalline heterodimers; [ag] perovskite oxide of La_2CuO_4; [ah] anchoring Cu single atoms with ultrathin porous Al_2O_3 with enriched Lewis acid sites; [ai] Cu/CeO_2 nanorod; [aj] nitrogen(N) and phosphorus(P)-doped copper(Cu).

References

1. Z. Xu, Q. Meng, Q. Cao, Y. Xiao, H. Liu, G. Han, S. Wei, J. Yan and L. Wu, *Anal. Chem.*, 2020, **92**, 2201-2206.
2. J. Yang, J. Yu, W. Dong, D. Yang, Z. Hua, X. Wan, M. Wang, H. Li and S. Lu, *Small*, 2023, **19**, 2301319.
3. W. Fang, R. Lu, F.-M. Li, C. He, D. Wu, K. Yue, Y. Mao, W. Guo, B. You, F. Song, T. Yao, Z. Wang and B. Y. Xia, *Angew. Chem. Int. Ed.*, 2024, **63**, e202319936.
4. D. Zhou, C. Chen, Y. Zhang, M. Wang, S. Han, X. Dong, T. Yao, S. Jia, M. He, H. Wu and B. Han, *Angew. Chem. Int. Ed.*, 2024, **63**, e202400439.
5. F. Pan, L. Fang, B. Li, X. Yang, T. O'Carroll, H. Li, T. Li, G. Wang, K.-J. Chen and G. Wu, *J. Am. Chem. Soc.*, 2024, **146**, 1423-1434.
6. M. Sun, Z. Tao, X. Xu, S. Min and L. Kang, *Appl. Catal. A Gen.*, 2023, **666**, 119406.
7. Y. Zhou, S. Chen, S. Xi, Z. Wang, P. Deng, F. Yang, Y. Han, Y. Pang and B. Y. Xia, *Cell Rep. Phys. Sci.*, 2020, **1**, 100182.
8. P. Yu, X. Lv, Q. Wang, H. Huang, W. Weng, C. Peng, L. Zhang and G. Zheng, *Small*, 2023, **19**, 2205730.
9. Y.-R. Wang, M. Liu, G.-K. Gao, Y.-L. Yang, R.-X. Yang, H.-M. Ding, Y. Chen, S.-L. Li and Y.-Q. Lan, *Angew. Chem. Int. Ed.*, 2021, **60**, 21952-21958.
10. Y.-R. Wang, H.-M. Ding, X.-Y. Ma, M. Liu, Y.-L. Yang, Y. Chen, S.-L. Li and Y.-Q. Lan, *Angew. Chem. Int. Ed.*, 2022, **61**, e202114648.
11. X.-Y. Dong, H. Chen, S. Wang, R.-Y. Zou, S.-Q. Zang and J. Cai, *Adv. Mater.*, 2025, **37**, 2413710.
12. Z. Weng, J. Jiang, Y. Wu, Z. Wu, X. Guo, K. L. Materna, W. Liu, V. S. Batista, G. W. Brudvig and H. Wang, *J. Am. Chem. Soc.*, 2016, **138**, 8076-8079.
13. T. Zhang, S. Verma, S. Kim, T. T. Fister, P. J. A. Kenis and A. A. Gewirth, *J. Electroanal. Chem.*, 2020, **875**, 113862.
14. Y. Cai, J. Fu, Y. Zhou, Y.-C. Chang, Q. Min, J.-J. Zhu, Y. Lin and W. Zhu, *Nat. Commun.*, 2021, **12**, 586.
15. H. Wu, B. Tian, W. Xu, K. K. Abdalla, Y. Kuang, J. Li and X. Sun, *J. Am. Chem. Soc.*, 2024, **146**, 22266-22275.
16. Q. Zhao, Y. Wang, M. Li, S. Zhu, T. Li, J. Yang, T. Lin, E. P. Delmo, Y. Wang, J. Jang, M. Gu and M. Shao, *SmartMat*, 2022, **3**, 183-193.
17. Z. Weng, Y. Wu, M. Wang, J. Jiang, K. Yang, S. Huo, X.-F. Wang, Q. Ma, G. W. Brudvig, V. S. Batista, Y. Liang, Z. Feng and H. Wang, *Nat. Commun.*, 2018, **9**, 415.
18. Y. Xu, F. Li, A. Xu, J. P. Edwards, S.-F. Hung, C. M. Gabardo, C. P. O'Brien, S. Liu, X. Wang, Y. Li, J. Wicks, R. K. Miao, Y. Liu, J. Li, J. E. Huang, J. Abed, Y. Wang, E. H. Sargent and D. Sinton, *Nat. Commun.*, 2021, **12**, 2932.
19. M. Li, F. Zhang, M. Kuang, Y. Ma, T. Liao, Z. Sun, W. Luo, W. Jiang and J. Yang, *Nano-Micro Lett.*, 2023, **15**, 238.
20. K. Zhang, J. Xu, T. Yan, L. Jia, J. Zhang, C. Shao, L. Zhang, N. Han and Y. Li, *Adv. Funct. Mater.*, 2023, **33**, 2214062.
21. W.-D. Zhang, Y. Zou, M. Chen, W. Jiang and X. Yan, *J. Alloys Compd.*, 2024, **978**, 173488.
22. S. Chen, W.-H. Li, W. Jiang, J. Yang, J. Zhu, L. Wang, H. Ou, Z. Zhuang, M. Chen, X. Sun, D.

Wang and Y. Li, *Angew. Chem. Int. Ed.*, 2022, **61**, e202114450.
23. A. Guan, Y. Fan, S. Xi, H. Huang, Q. Zhang, N. Lyu, B. Wu, Y. Chen, Z. Liu, C. Yang, Y. Ji, M. Kan, L. Zhang and G. Zheng, *ACS Mater. Lett.*, 2023, **5**, 19-26.
24. S. Roy, Z. Li, Z. Chen, A. C. Mata, P. Kumar, S. C. Sarma, I. F. Teixeira, I. F. Silva, G. Gao, N. V. Tarakina, M. G. Kibria, C. V. Singh, J. Wu and P. M. Ajayan, *Adv. Mater.*, 2024, **36**, 2300713.
25. Y. Dai, H. Li, C. Wang, W. Xue, M. Zhang, D. Zhao, J. Xue, J. Li, L. Luo, C. Liu, X. Li, P. Cui, Q. Jiang, T. Zheng, S. Gu, Y. Zhang, J. Xiao, C. Xia and J. Zeng, *Nat. Commun.*, 2023, **14**, 3382.
26. M. K. Kim, H. J. Kim, H. Lim, Y. Kwon and H. M. Jeong, *Electrochim. Acta*, 2019, **306**, 28-34.
27. Y. Zhang, L.-Z. Dong, S. Li, X. Huang, J.-N. Chang, J.-H. Wang, J. Zhou, S.-L. Li and Y.-Q. Lan, *Nat. Commun.*, 2021, **12**, 6390.
28. R. Wang, J. Liu, Q. Huang, L.-Z. Dong, S.-L. Li and Y.-Q. Lan, *Angew. Chem. Int. Ed.*, 2021, **60**, 19829-19835.
29. H. Zou, G. Zhao, H. Dai, H. Dong, W. Luo, L. Wang, Z. Lu, Y. Luo, G. Zhang and L. Duan, *Angew. Chem. Int. Ed.*, 2023, **62**, e202217220.
30. P. Zhao, H. Jiang, H. Shen, S. Yang, R. Gao, Y. Guo, Q. Zhang and H. Zhang, *Angew. Chem. Int. Ed.*, 2023, **62**, e202314121.
31. J. Zhao, P. Zhang, T. Yuan, D. Cheng, S. Zhen, H. Gao, T. Wang, Z.-J. Zhao and J. Gong, *J. Am. Chem. Soc.*, 2023, **145**, 6622-6627.
32. Y. Wang, Z. Chen, P. Han, Y. Du, Z. Gu, X. Xu and G. Zheng, *ACS Catal.*, 2018, **8**, 7113-7119.
33. S. B. Varandili, J. Huang, E. Oveisi, G. L. De Gregorio, M. Mensi, M. Strach, J. Vavra, C. Gadiyar, A. Bhowmik and R. Buonsanti, *ACS Catal.*, 2019, **9**, 5035-5046.
34. S. Chen, Y. Su, P. Deng, R. Qi, J. Zhu, J. Chen, Z. Wang, L. Zhou, X. Guo and B. Y. Xia, *ACS Catal.*, 2020, **10**, 4640-4646.
35. S. Chen, B. Wang, J. Zhu, L. Wang, H. Ou, Z. Zhang, X. Liang, L. Zheng, L. Zhou, Y.-Q. Su, D. Wang and Y. Li, *Nano Lett.*, 2021, **21**, 7325-7331.
36. L. Xue, C. Zhang, J. Wu, Q.-Y. Fan, Y. Liu, Y. Wu, J. Li, H. Zhang, F. Liu and S. Zeng, *Appl. Catal. B Environ. Energy*, 2022, **304**, 120951.
37. Z. Li, Y. Yuan, G. Qu, K. Xiang, P. Ning, W. Du, K. Pan, Y. Cai and J. Li, *Appl. Catal. B Environ. Energy*, 2025, **360**, 124525.